ISSN 1068-3755, Surface Engineering and Applied Electrochemistry, 2018, Vol. 54, No. 6, pp. 562–576. © Allerton Press, Inc., 2018.

Instability of Ferrous Sulfate Bath for Electrodeposition of Nanocrystalline Iron Coating[1]

A. Bahrololoomi[a] and M. E. Bahrololoom[a, *]

[a] *Department of Materials Science and Engineering, Shiraz University, Shiraz, Iran*

**e-mail: bahrolom@shirazu.ac.ir*

Received December 15, 2017

Abstract—Nanocrystalline iron coatings were electrodeposited at six different current densities, from 1 to 25 A dm^{-2} from a bath containing iron(II) sulfate at 60 and 80°C. The impact of the current density on the bath deterioration was investigated. The bath color changed from emerald green (485 nm maximum absorption wavelength, λ_{max}) to turbid yellow (λ_{max} = 470 nm) with some orange precipitates after electrodeposition up to 10 A dm^{-2}. Further electrodeposition up to 25 A dm^{-2} changed the bath colour to dark brown (λ_{max} = 435 nm). Ultraviolet-Visible spectra were recorded to verify the bath deterioration, which, in turn, prevented the coating growth. The color change and also the shift of the maximum absorption wavelength were discussed in terms of the crystal field theory and also of the anodic oxidation of the hexaaquairon(II) ion to the hexaaquairon(III) ion on the anode surface. The Pourbaix diagram for iron was used to interpret these results and the instability of the bath which was utilized here for electrodeposition of nanocrystalline iron coatings. Addition of saccharin also led to the bath instability. The influence of the bath instability on the average grain size, appearance, surface morphology and thickness of the coatings was discussed. The results proved that the iron(II) sulfate solution is an unstable bath for electrodeposition of nanocrystalline iron coatings.

Keywords: electrodeposition, nanocrystalline iron, bath instability, crystal field theory, Pourbaix diagram, saccharin

DOI: 10.3103/S1068375518060029

INTRODUCTION

The earliest attempt to electrodeposit iron coatings was apparently in the middle of the 19th century [1]. In view of the fact that electrodeposited iron has some valuable properties, it has been used for several applications, for instance, engraved plates [2, 3], in manufacturing new machine parts [4] and recently its usage as a new biomaterial for stents has been reported and a process for electroforming form a chloride bath containing saccharin for its production was developed [5, 6]. Some research in the field of iron electrodeposition was reported including studies of mechanical [7] and magnetic [8, 9] coating properties. Iron electrodeposition usually takes place from plating baths containing iron(II) salts such as sulfate, chloride, fluoborate, and sulfamate [10, 11]. Over the past forty years, there have been extensive studies of iron coatings electrodeposited from different baths. The authors in [12] investigated the influence of the current density, solution temperature and pH on the quality of iron electroformed from chloride baths. Their conclusion was that the current efficiency is decreased when current density increases. Another group of researchers who worked on the structure, the grain size, the internal stress, and the mechanical properties of iron foils electrodeposited from a sulfate bath reported the grain size of 5 μm produced at a low current density (3 A dm^{-2}) and 0.1 μm at current densities higher than 20 A dm^{-2}. Their results showed that the size of grains is reduced by increasing the current density [7]. Still others investigated the mechanical, magnetic, and electrical properties of electrodeposited iron foils made from a chloride bath [1] and from a sulfate bath [13].

Recently, nanocrystalline metals and alloys, due to their excellent properties and various applications, and nanocrystalline iron coatings formed from a sulfate bath via both direct and pulsed current electrodeposition in order to investigate the influence of nanocrystallinity on the corrosion behavior of iron coatings, have been the subjects of extensive research [14–16]. The authors have also demonstrated that, according to the Hall-Petch strengthening mechanism, nanocrystalline coatings show significant increases in hardness and strength relative to larger grained deposits due to their ultrafine grain size. Unfortunately, high current densities that are often used for electrodeposition of nanocrystalline iron coatings can lead to the instability of the electrolyte and consequently change the desirable chemical conditions required for electrodeposi-

[1] The article is published in the original.

tion. Thus, the stability of electroplating baths during electrodeposition is very important.

Lack of the bath stability usually yields poor quality coatings and for some plating baths the chemistry is changed so much that the baths do not produce any coating. Factors which may lead to the instability of a bath include ligand exchange reactions [17] and pH changes [10] during electrolysis of an aqueous bath, which can alter the bath chemistry. Another factor that changes the concentration of metallic ions during electrodeposition and consequently gives instability to a plating bath is the undesired anodic oxidation of the metallic ion present in the bath to its higher oxidation state [18]. This is true for metals such as iron that have different ions and oxidation states. Some researchers have studied the stability of the baths used for electrodeposition of various metals. For example, lack of the bath stability in non-cyanide baths for electrodeposition of gold has been reported in which colloidal gold is formed in the plating solution and these colloidal particles are deleterious to the electrodeposited gold coatings [19, 20]. The stability of copper complex ions in electrolytes has also been studied, although not for copper electroplating, and spectrophotometric analysis of the electrolyte has been performed to characterize different copper complex ions in the solution [21]. The problem of bath instability is real during electrodeposition of iron from iron(II) sulfate solutions. Electrochemistry of iron salts solutions is dominated by the +2 and +3 oxidation states. At the anode, the iron(II) ion is oxidized to the iron(III) ion during electrolysis of iron(II) sulfate solutions. Presuming that the anodic oxidation of the iron(II) ion to the iron(III) ion is a reason for the instability of the iron plating baths, it is possible to forecast that, such instability would be accelerated when high current densities are used for electrodeposition of iron. When the iron(III) ion is formed at the anode in the bath, the concentration of the iron(II) ion required for electrodeposition is reduced. An obvious consequence will be lowering the cathodic current efficiency of iron deposition. The rate of the electrolytic conversion of the iron(II) ion to the iron(III) ion is not the same when different anodes are used. It was reported that this rate is controlled by mass transport to the anode surface [22]. It seems that very few researchers have paid enough attention to this electrochemical reaction that leads to the instability of iron plating baths. For instance, the author of [10] just mentioned the observed bath instability during electrodeposition of iron but did not give any evidence of this problem. Some investigators worked on the grain size and morphology of electrodeposited iron foils produced from a chloride bath with organic additives such as sodium saccharin, at high current densities and with additions of different cations [23]. Their results showed that the grain size of pure iron was over 100 nm but, and that adding cations such as manganese (Mn), lanthanum (La) and samarium (Sm) ions can result in an extreme range of grain sizes (about 33.6 to 97.4 nm) could be obtained. Different additives like sodium saccharin [24] and glycine [25] were used to enhance protection of coatings against air oxidation. Addition of these additives improved the quality of their deposits. Recently, iron foils have been electroformed from a chloride bath with 1 g L^{-1} sodium saccharin for application as biodegradable cardiovascular stent [5].

The aim of the present research was to study the bath instability during electrodeposition of nano-crystalline iron coatings, which has not been reported extensively so far, to the best of authors' knowledge, although it was been briefly mentioned in [10]. The difficulties with electrodeposition of iron come from the instability of iron plating baths, which can be summarized as follows: rapid pH increase during electrodeposition; formation and decomposition of complex ions (ligand exchange reactions), and anodic oxidation of the iron(II) ion, which must be reduced to produce metallic iron.

The appearance, morphology and cross sections of the coatings which are influenced by the bath instability are reported in this manuscript. In addition, close attention was paid to the effect of saccharin and high temperature on the bath instability. Changes in the bath color, formation of precipitates and also spectroscopic studies of the plating baths were used as the main criteria for the bath instability. The results of the ultraviolet-visible (UV-Vis) spectroscopy analyses were interpreted on the base of ligand exchange reactions and the crystal field theory.

MATERIALS AND METHODS

Electrodeposition was carried out in these experiments with direct currents and at two different temperatures 60 and 80°C. The plating time for each sample was 10 minutes. The bath contained 500 g L^{-1} iron(II) sulfate. Bearing in mind that saccharin can act as grain refiner for nickel plating [26–29], in electrodeposition of iron coatings of the present investigation, 10 g L^{-1} saccharin was added to the baths for electrodeposition of iron coatings of the present investigation. The bath pH was about 2.5. Different current densities (1, 5, 10, 15, 20 and 25 A dm^{-2}) were used. The substrates were copper foils, each of 0.1 mm thickness and 5 cm^2 (2 × 2.5 cm) surface area. Apart from the required area (5 cm^2) for electrodeposition, the copper substrates were coated with a lacquer paint in order to make it non-conductive. Next, the conductive surface of each sample was polished with 180 to 3000 grade abrasive paper (emery) and then electropolished in a solution containing phosphoric acid (75 mL), ethanol (75 mL) and water (150 mL). Immediately after being electropolished, the samples were washed with distilled water. A piece of graphite was used as a non-consumable anode. The instability of the iron(II) sulfate baths during electrodeposition was

investigated by visual observation of changes in the color of the solution and of the precipitates formed during electrodeposition. Any color change is an indication of hydrated metallic ions formed in the solution. The color change was also confirmed by UV-Vis, with 500 gram per liter concentration and the path length of 1 centimeter. The UV-Vis spectra were recorded before and after electrodeposition and the shift of the absorption peak was taken as an indication of the color change of the solution and, hence, the instability of the bath. Optical microscopy was used to measure the thickness of the coatings. Appearance of the coatings was observed visually and their photographs were taken by a digital camera. Scanning electron microscopy was used to study the surface morphology. X-ray diffraction (XRD) data analyses with X-pert Pro and SigmaPlot software were used to determine the grain size. The Williamson-Hall equation was used to calculate the average grain size (Eq. 1) [30]:

$$\beta\cos\theta = \frac{0.9\lambda}{d} + 2A\varepsilon\sin\theta, \quad (1)$$

where λ is the X-ray wavelength of copper (λ = 1.5406 Å), β is the peak width, d is the crystallite size (nm), A is a constant which is often equal to 1, ε is the microstrain of the coatings and θ is the diffraction angle.

In order to determine the cathodic current efficiency, the theoretical weight of each deposit was calculated based on Faraday's law (Eq. (2)).

$$W_{\text{th}} = \frac{Mit}{nF}. \quad (2)$$

This equation is used when a pure metal is electrodeposited. In the present investigation, it was observed that initially pure iron is electrodeposited and then iron oxide is formed on the previously electrodeposited pure iron. Consequently, the coating is an iron oxide top-layer on a pure iron under-layer. Thus, Eq. (2) was modified to a new form (Eq. (3)) in order to be used for the situation when pure iron and iron oxide are formed since the amount of iron oxide was different from one sample to another.

$$W_{\text{th}} = \frac{\left(\left(M_{\text{Fe}} \times \%\text{Fe}\right) + \left(M_{\text{Fe}_3\text{O}_4} \times \%\text{Fe}_3\text{O}_4\right)\right) it}{nF}. \quad (3)$$

The percentage of iron oxide for each sample, determined from its corresponding XRD spectrum, was inserted in Eq. (3) to calculate the theoretical weight of that sample. The cathodic current efficiency, η, was calculated by using Eq. (4):

$$\eta = \frac{W_{\text{exp}}}{W_{th}} \times 100, \quad (4)$$

where W_{th} is the theoretical weight (g) of the deposit, W_{exp} is the experimental weight of the deposit, M is the molar mass of the substance (g mol), i (A) is the current flowing through the plating solution, t is time duration (s), n is the valence number of ions of the substance (electrons transferred for each ion), F is the Faraday constant (F = 96500 C mol^{-1}) and η is the cathodic current efficiency percentage.

RESULTS AND DISCUSSION

Grain Size

Figure 1 shows the XRD spectra of the samples electrodeposited with a range of current densities from 1 to 25 A dm^{-2} with increments of 5 A dm^{-2}. The fraction of iron and iron oxide, which was used in Eq. (3) to calculate the theoretical weight of the samples, was extracted from the intensity of peaks in the XRD spectra. Based on the observation of the appearances of the coatings, it should be mentioned that increasing the current density from 1 to 10 A dm^{-2} resulted in producing a metallic coating surface, which indicated the electrodeposition of iron. However, at 15 to 25 A dm^{-2}, the coating surface was dark. This indicates that iron oxide was formed on the surface. There was not noticed any overlapping of peaks up to 10 A dm^{-2} which was due to iron peaks. Although, overlapping of peaks for iron and iron oxide is observed at 15 up to 25 A dm^{-2}, the peaks being, mostly, due to iron oxide. The peak occurring at 44.7 degrees was chosen to be as a criterion for the discussion of the grain size of the electrodeposited iron. The iron peak intensity decreased but its width increased, with increasing the current density from 1 to 10 A dm^{-2}.

By using Eq. (1), the average grain sizes were calculated for the samples electrodeposited with the above current densities and are shown in Table 1. The data indicate that increasing the current density from 1 to 10 A dm^{-2} resulted in reducing the grain size. At current densities from 15 to 25 A dm^{-2}, the iron peak intensity overlapped with that of the peak formed due to iron oxide. It was also observed that the iron oxide (magnetite) peak had a high intensity, with its sharpness increasing. The peak for iron oxide (magnetite) was pronounced, indicating oxidation of the coated samples electrodeposited at 15 to 25 A dm^{-2}.

The size of the grains of the samples (see Fig. 2) prepared at 10 to 25 A dm^{-2} increased by increasing the current density. As a rule, the size of the grains decreases when the current density increases but it did not occur here, indicating that electrodeposition from 1 to 10 A dm^{-2} produced iron and the calculated grain size was due to the iron crystallite size (Region I in Fig. 2). However, iron oxide was produced at 10 to 25 A dm^{-2} (Region II in Fig. 2), and the calculated grain size was corresponding to the iron oxide crystallite size which cannot be compared with the grain size of nanocrystalline pure iron. Iron and iron oxide, being two different types of materials, have different crystallographic

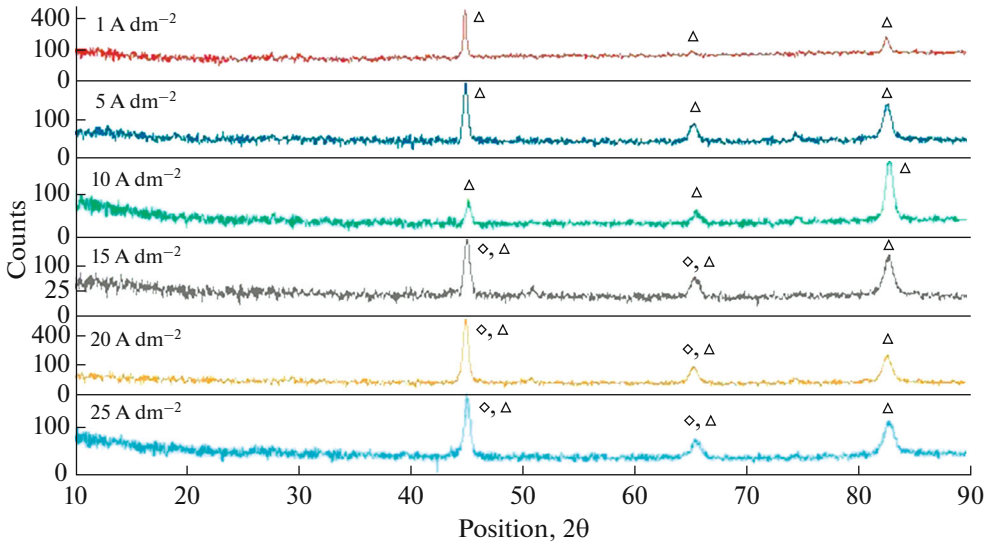

Fig. 1. XRD patterns of iron coatings obtained at different current densities at 60°C. The symbols correspond to Fe (△) and Fe_3O_4 (◇).

structures. Thus, they cannot be compared with each other regarding their nanocrystallinity.

Figure 3 shows the XRD patterns of iron coatings obtained at different current densities (i.e. 1, 5 and 20 A dm^{-2}) at two different temperatures. The XRD peak (at 44.7 degrees) for the iron oxide electrodeposited at 20 A dm^{-2} and 80°C was sharper than that for the iron oxide coating electrodeposited at 60°C and the same current density. The average grain sizes of the deposits decreased at higher current densities for both temperatures.

Figure 4 shows that the variation of the average grain size with increasing the current density (slope of the dotted line) is steep from 1 to 5 A dm^{-2} at 60°C but when the current density is changed from 5 to 20 A dm^{-2}, the slope is approximately constant. At 80°C, the slope of the solid line from 1 to 5 A dm^{-2} is not as steep as that at 60°C and the same current densities. However, when the current density is changed from 5 to 20 A dm^{-2} at 80°C, the slope is relatively steep, implying a decrease in the average grain size.

Figure 5 shows the XRD spectra of the samples electrodeposited at 5 and 20 A dm^{-2} from the bath with and without saccharin. Deposits were not produced at a low current density (1 A dm^{-2}). The iron peak (at 44.7 degrees) was sharp for the sample elec-

Table 1. Calculated values for the grain size of iron coatings obtained at different current densities

Current density, A dm^{-2}	Temperature, °C	Saccharin, 10 g L^{-1}	Average grain size, nm
1	60	No	107
5	60	No	78
10	60	No	21
15	60	No	32
20	60	No	73
25	60	No	127
1	80	No	127
5	80	No	116
20	80	No	82
1	60	Yes	Deposits were not produced
5	60	Yes	87
20	60	Yes	Iron peak had low intensity

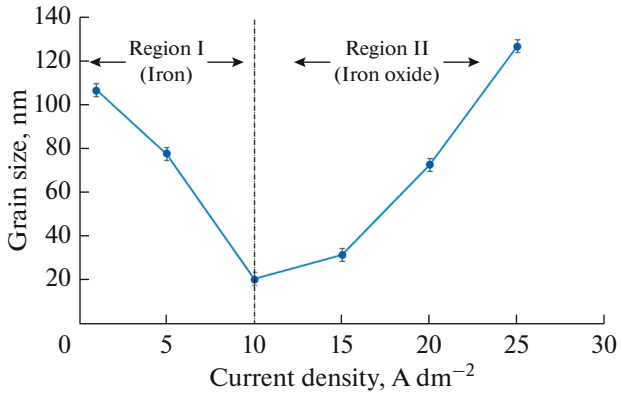

Fig. 2. Influence of different current densities on average grain size of iron coatings at 60°C.

trodeposited at 5 A dm^{-2} from the bath without saccharin. It should be mentioned that copper peaks were detected on the XRD spectra of the samples electrodeposited at 5 A dm^{-2} from the bath with saccharin. It is evident from the results that at 20 A dm^{-2} with saccharin, the copper peaks were sharp and the iron peak was diminished. The average grain sizes of iron coatings at the mentioned current densities (Table 1) revealed the fact that adding saccharin, increases the grain size. Thus, it can be concluded that saccharin does not act as a grain refiner for electrodeposition of iron. This is in contrast to its role as a grain refiner in nickel plating [29]. It seems that addition of saccharin to the iron plating bath is not beneficial. It prohibits iron deposition and apparently leads to the bath instability.

Bath Instability

The freshly prepared iron(II) sulfate bath was clear emerald green before electrolysis. It turned into a turbid yellow solution with some orange precipitates after 10 minutes of electrolysis at four different current densities: 1, 5, 10 and 15 A dm^{-2}. Further electrodeposition at 20 and 25 A dm^{-2} changed the bath color to dark brown containing yellow precipitates which were produced on the graphite anode during electrodeposition. UV-Visible spectra (Fig. 6) were recorded to verify these color changes that are indicative of the bath instability, which, in turn, prevents further increase of the coating thickness.

The solid line (curve *1*, Fig. 6) is the spectrum of the iron(II) sulfate bath before electrolysis. Each vertical line passes over the maximum absorption wavelength of each solution. It shows that, the maximum absorption wavelength of the original bath before electrodeposition (curve *1*) occurs at about 485 nm. This maximum absorption wavelength (λ_{max}) in the visible spectrum corresponds to the emerald green hexaaquairon(II) ion, $\left[Fe\left(H_2O\right)_6\right]^{2+}_{(aq)}$. When four samples were electrodeposited for 10 min each, at 1, 5, 10 and 15 A dm^{-2}, the bath color changed from emerald green to yellow-orange. This was manifested by the shift of absorption from spectrum *1* to spectrum *2* in Fig. 6. The maximum absorption wavelength (λ_{max}) shifted from 485 to 470 nm, shown by a small arrow. The change in color, accompanied by the shift of λ_{max} from 485 to 470 nm is due to the anodic oxidation of hexaaquairon(II) ion on the anode surface and formation of hexaaquairon(III) ion, $\left[Fe\left(H_2O\right)_6\right]^{3+}_{(aq)}$ which is pale yellow.

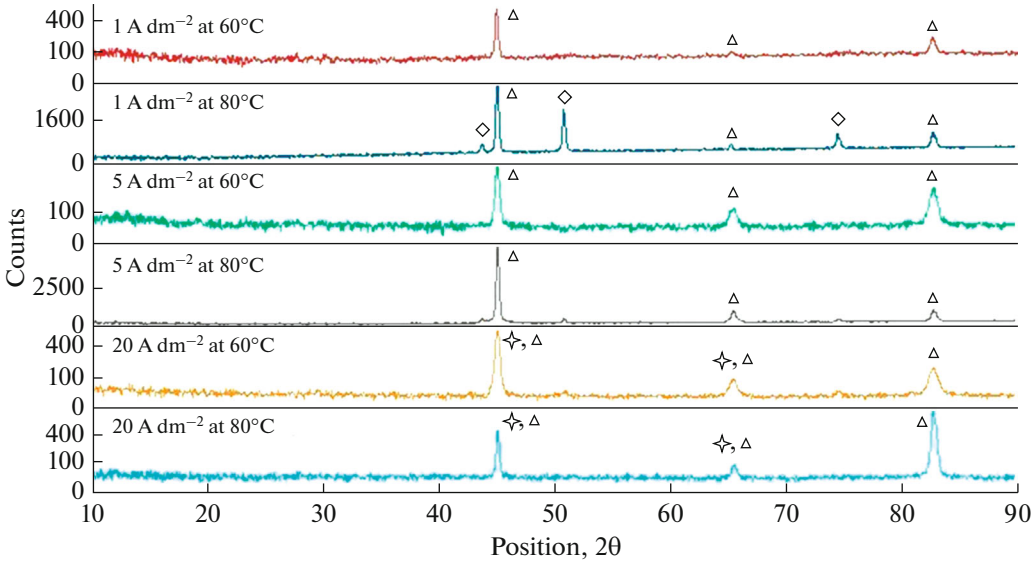

Fig. 3. XRD patterns of iron coatings obtained at different current densities and two different temperatures. The symbols are: (△) for Fe, (✧) for Fe_3O_4 and (◇) for Cu.

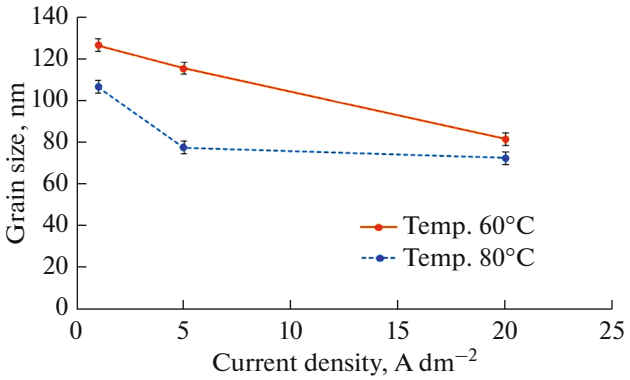

Fig. 4. Influence of three different current densities on average grain size of iron coatings at two different temperatures.

However, this trivalent ion is not the only species in aqueous solutions. The observed yellow-orange color is due to a proton transfer process in which a hydroxo-complex ion is formed, as shown in Eq. (5):

$$\left[Fe\left(H_2O\right)_6\right]^{3+}_{(aq)} + H_2O_{(l)} \rightarrow \left[Fe\left(H_2O\right)_5OH\right]^{2+}_{(aq)} + H_3O^{+}_{(aq)}. \quad (5)$$

With further electrodeposition, the bath pH increases gradually and the above proton transfer process can continue at a higher pH of the medium to form the iron(III) hydroxide precipitate which is dark brown. Thus, electrodeposition of other two samples at 20 and 25 A dm^{-2}, each plated for 10 min, changed the color of the solution to dark brown. This was accompanied by shifting the visible spectrum to curve *3* (the thick dotted line) in Fig. 6. The maximum absorption wavelength (λ_{max}) shifted to 435 nm (the long arrow), which corresponds to dark brown color of the solution.

The hydroxo-complex ion formed as in Eq. (5) can lose a second hydrogen ion and a third hydrogen ion, as shown in Eqs. (6) and (7):

$$\left[Fe\left(H_2O\right)_5OH\right]^{2+}_{(aq)} \rightleftarrows \left[Fe\left(H_2O\right)_4\left(OH\right)_2\right]^{+}_{(aq)} + H^{+}_{(aq)}; \quad (6)$$

$$\left[Fe\left(H_2O\right)_4\left(OH\right)_2\right]^{+}_{(aq)} \rightleftarrows \left[Fe\left(H_2O\right)_3\left(OH\right)_3\right]_{(s)} + H^{+}_{(aq)}. \quad (7)$$

The solid formed as in Eq. 7 is a neutral complex and it precipitates in water which makes the solution turbid. Most hydroxo species of iron are yellow because of charge-transfer bands in the ultraviolet radiation which extends into the visible part of the electromagnetic spectrum. When electrodeposition takes place, all complexes of iron that were explained in the above equations are present in the iron plating bath. The proportions depend on the degree of concentration of the solution, on the current densities used for electrodeposition, and on the time of plating. Therefore, the color of the bath is variable and depends, in part, on the concentration of the iron(III) ion, which is low, and when this is the only species of iron present in the solution, the color is pale yellow.

A solution with a higher concentration of the iron(III) ions is orange and produces some orange precipitate [18].

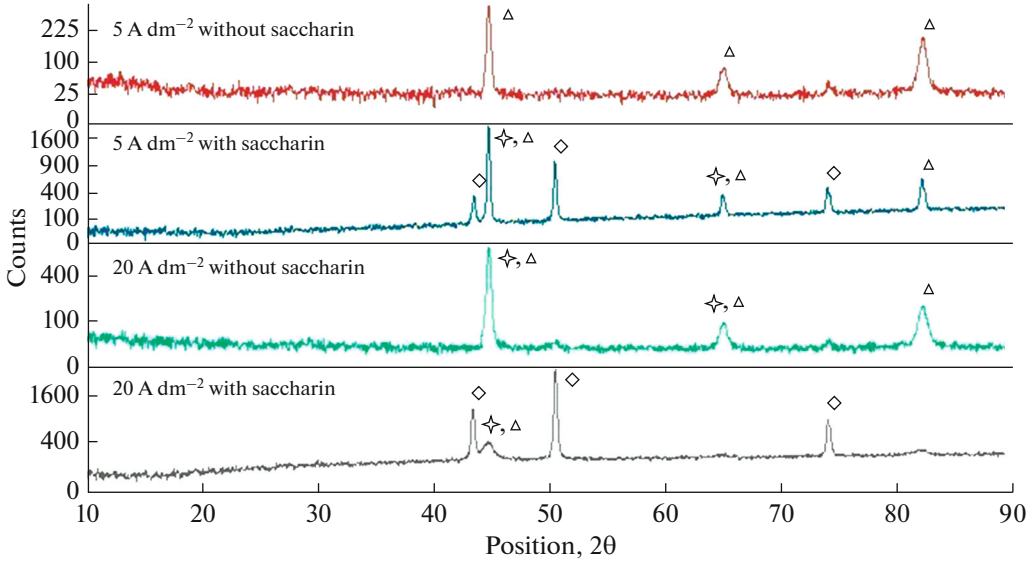

Fig. 5. XRD patterns of iron coatings obtained from different current densities with and without saccharin at 60°C. The symbols correspond to Fe (△), Fe_3O_4 (✧), and Cu (◇).

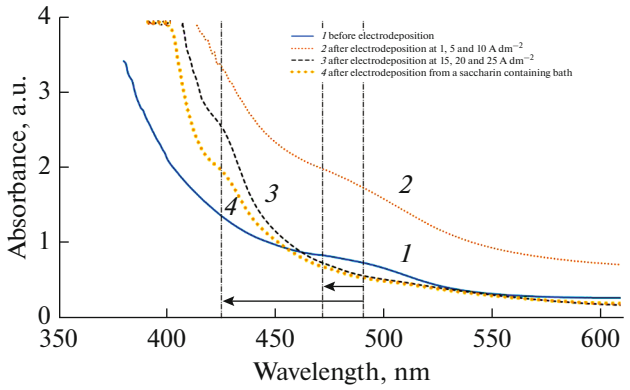

Fig. 6. UV-Vis spectra of iron plating baths before and after electrodeposition at different current densities.

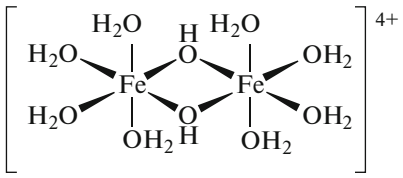

Fig. 7. Structure of binuclear iron hydroxo complex ion.

Another factor that leads to the instability of iron(II) sulfate baths for electrodeposition of iron is its vulnerability to air oxidation. The oxidation potential of Fe^{2+} ion to Fe^{3+} ion (0.77 V) is such that molecular oxygen can convert a ferrous ion into a ferric ion in an acidic environment. This is shown in Eq. (8):

$$2Fe^{2+}_{(aq)} + \frac{1}{2}O_{2(g)} + 2H^{+}_{(aq)} \rightleftarrows 2Fe^{3+}_{(aq)} + H_2O_{(l)}; \quad E^\circ = 0.46\ \text{V}. \tag{8}$$

The above reaction can also be written as a reaction between oxygen and ferrous hydroxide:

$$4Fe(OH)_{2(s)} + O_{2(g)} + 2H_2O_{(l)} \rightarrow 4Fe(OH)_{3(s)}. \tag{9}$$

Thus, ferrous hydroxide becomes dark orange brown (rust-colored) when it precipitates in the presence of air and eventually it is converted into hydrous ferric oxide $Fe_2O_3 \cdot nH_2O$ (n is variable). Ferrous hydroxide and ferric hydroxide are neutral complexes, i.e. $[Fe(OH)_2(H_2O)_4]$ and $[Fe(OH)_3(H_2O)_3]$. Displacement of water molecules with hydroxide, (OH^-) ions is a ligand exchange reaction which leads to the formation of precipitates in the iron plating bath and causes its instability. The ligand exchange reactions (OH^- for H_2O) are deprotonation reactions; the electrical charge on the complex is reduced by 1 for each proton transferred when an electrically neutral water ligand is replaced by a charged hydroxide ion (OH^-) ligand. In these deprotonation reactions, water acts as a Brönsted–Lowry base which accepts a proton and the hexaaqua ion acts as a Brönsted–Lowry acid which donates a proton. As explained above, the iron(III) ion in an aqueous solution forms many complexes. One of these complexes is a binuclear complex formed as shown in Eq. (10) [17]:

$$2\left[Fe(H_2O)_6\right]^{3+}_{(aq)} \rightleftarrows \left[Fe(H_2O)_4(OH)_2Fe(H_2O)_4\right]^{4+}_{(aq)} + 2H_2O_{(l)} + 2H^{+}_{(aq)}. \tag{10}$$

The above binuclear complex ion has the structure shown in Fig. 7.

Evidently, formation of iron(III) complexes such as that in the above Equation interferes with the process of iron electrodeposition and plays a major role in the instability of the iron plating bath. Perhaps, a comparison can be made of the visible adsorption maxima and also the solution color for the hexaaquairon(II) complex ion and the hydroxo complex of the iron(III) ion. This comparison is summarized and shown in Table 2.

According to the crystal field theory, the degenerate d orbitals of iron(II) ion split into a doubly degenerate high energy level (e_g) and a triply degenerate low energy level (t_{2g}) [17, 18]. The energy difference (Δ_o) is known as the d-orbital splitting energy and the subscript "O" stands for "octahedral complex." Absorption of light corresponds to the energy required (Δ_o) to excite an electron from the t_{2g} level to the e_g level. The magnitude of Δ_o depends both upon the oxidation state of iron (+2 and +3) and on the attaching ligands in the octahedral complex. Δ_o is higher for Fe^{3+} ion than for Fe^{2+} ion. For the hexaaquairon(III) complex ion, the degenerate d^5 orbital splits into e_g and t_{2g} levels

Table 2. Complexes of different oxidation states of iron with their maxima absorption wavelengths and observed colors

Iron oxidation states	Ion complexes	Wavelength of light absorbed, nm	Color of light absorbed	Color seen
Iron(II) ion	$[Fe(H_2O)_6]^{2+}$	750 and 485 (The main absorption bands)	Red	Green
Iron(III) ion	$[Fe(H_2O)_5OH]^{2+}$	470	Blue	Yellow-orange
Iron(III) ion	$[Fe(H_2O)_4(OH)_2]^{+}$	435	Violet	Yellow

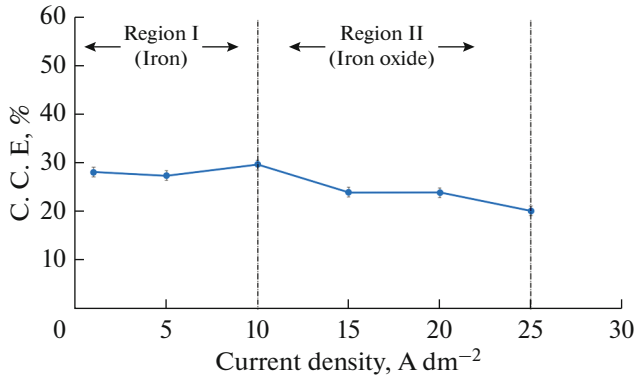

Fig. 8. Cathodic current efficiency of iron coatings obtained at 60°C and different current densities.

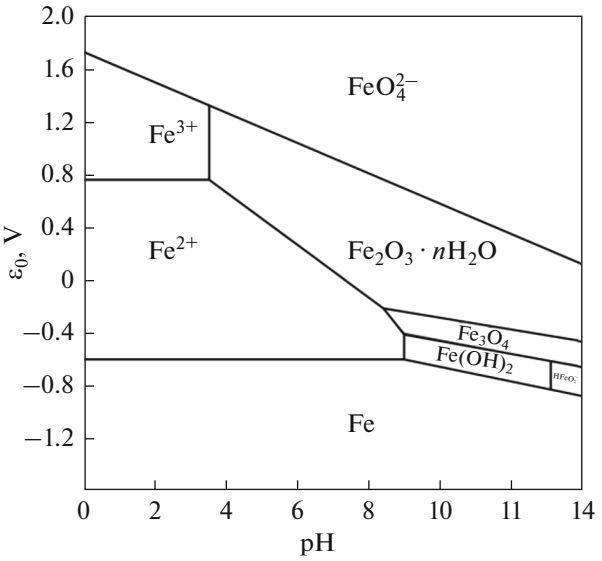

Fig. 9. The Pourbaix diagram of iron [31].

and Δ_o for splitting of this ion is higher than Δ_o for splitting of hexaaquairon(II) complex ion. Since Δ_o is higher for Fe^{3+} ion than for Fe^{2+} ion, the hexaaquairon(III) complex ion absorbs higher energy from the visible light (blue color) and thus its solution is yellow-orange and its maximum absorption wavelength (λ_{max}) shifts to lower wavelength values, as seen in Fig. 6. It should be remembered that the original iron(II) sulfate bath, used for electrodeposition of iron in the present investigation, contained hexaaquairon(II) complex. When electrodeposition was performed some hexaaquairon(III) complex was produced due to the anodic oxidation of Fe^{2+} ion to Fe^{3+} ion. The amount of the produced hexaaquairon(III) complex depends on the current density and the time of electrodeposition. Thus, the bath color after electrodeposition is a mixed-color due to the presence of both oxidation states of iron in the bath. The recorded visible spectrum is also an overlapping of different absorption bands due to the presence of all complexes in the bath. For the same ligand, a metal ion with a higher oxidation state will produce a greater crystal field splitting. Solutions of iron(III) complexes are yellow or red while iron(II) complexes are pale green. This is because as the oxidation state of the metal increases the magnitude of the energy difference (Δ_o) between the splitted *d* orbitals increases and hence the wavelength of the absorption moves towards a lower wavelength, i.e. a higher energy. For iron(III) complexes, the absorption moves towards the blue end of the spectrum and, consequently, their solutions are yellow or red.

Electrodeposition of iron is usually carried out from the iron(II) sulfate solution but electrolysis of this bath causes oxidation of the iron(II) ions to the iron(III) ions on the anode and forms on it the iron(III) oxide (ferric oxide) precipitates. Consequently, the iron(II) ion concentration in the bath decreases. This phenomenon prevents or retards reduction of the iron(II) ion on the cathode and decreases the cathodic current efficiency. The maximum cathodic current efficiency was 29.83% at 10 A dm^{-2}, but it decreased at a higher current density, and the minimum cathodic current efficiency was 20.43% at 25 A dm^{-2} (Fig. 8). This trend of the cathodic current efficiency is in good agreement with some earlier reports [1, 12].

This instability can be explained rationally in terms of electrochemistry of iron species in aqueous solutions and vulnerability of metallic iron and of its divalent cation to oxidation. As the following equation shows, the reduction potential of the iron(II) ion is –0.44 V [31]:

$$Fe^{2+}_{(aq)} + 2e^- \rightarrow Fe_{(s)};\ E^\circ = -0.44\ \text{V}. \qquad (11)$$

Instability of the iron plating bath can be discussed on the base of the Pourbaix diagram for iron (Fig. 9). According to this diagram, iron(II) ions are reduced to pure iron at –0.44 V reduction potential. During electrodeposition, when iron(III) is formed on the anode, hydrogen ions are reduced on the cathode and hydrogen gas is evolved. Consequently, the bath pH increases in the vicinity of the cathode. As a result, iron oxide (magnetite) is formed when the bath pH shifts from 8.5 to 14, as seen in Fig. 9. Higher current densities accelerate formation of iron oxide.

When electrodeposition was carried out at 80°C, the bath color quickly turned to a turbid yellow, with too much of the suspended orange precipitate; this is why it could not be studied with the UV-Vis spectroscopy because the precipitates could contaminate the UV-Vis cell. It should be noted that any solid contamination in the spectrometer cell diffracts the ultraviolet ray. Increasing current density stabilized the precipitates which turned to black at high current densities. As seen in Fig. 10, the cathodic current efficiency at different current densities (i.e. 1, 5 and 20 A dm^{-2}) were determined at 60 and 80°C. The maximum

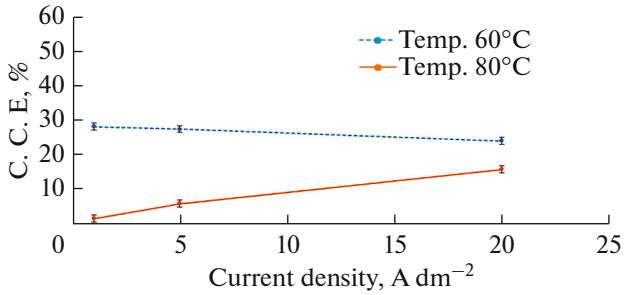

Fig. 10. Cathodic current efficiency of iron coatings at two different temperatures and different current densities: 1, 5 and 20 A dm^{-2}.

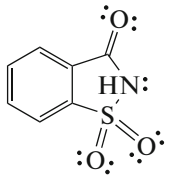

Fig. 11. Molecular structure of saccharin with lone pairs of electrons on nitrogen atom and oxygen atoms.

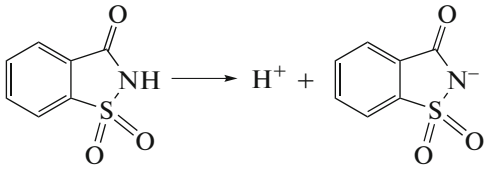

Fig. 12. Deprotonation reaction of saccharin to produce saccharinato anion.

cathodic current efficiency was 28.4% at 1 A dm^{-2} and 60°C. It decreased with increasing current density. However, the bath efficiency was minimum at this current density (1 A dm^{-2}) and at 80°C. In contrast, the cathodic current efficiency increased by increasing current density when deposition took place at 80°C.

The original iron(II) sulfate bath was clear emerald green before electrolysis. Addition of saccharin deteriorated the bath and changed its color and perhaps its chemical composition as implied by the shift of maximum absorption of the UV-Vis spectrum (curve *4* in Fig. 6). Furthermore, some small particles were also formed in the solution. After electrolysis at different current densities, i.e. 1, 5 and 20 A dm^{-2}, the particles were produced rapidly when increasing the current density. It is apparent that adding saccharin to the bath for electrodeposition of nanocrystalline iron can be very deleterious with regards to the bath stability and also the composition and quality of the coating. This might be due to the occurrence of a reaction between iron(II) ions and saccharin as a result of the complex ion formation if saccharin could act as ligand rather than as grain refiner. The imino group and the carbonyl group in saccharin have the ability to form a complex ion with Fe^{2+} ion present in the bath. The nitrogen atom with a pair of electrons serves as the donor atom in a great variety of ligands. Each oxygen atom in the carbonyl group and the sulfonyl group has also two lone pairs of electrons with ability to form complex ions, as shown in the structure of saccharin molecule (Fig. 11).

Deprotonation reaction of saccharin produces an anion (saccharinato anion), with the structure shown in Fig. 12, which can form a complex ion with the transition metal cations [17].

The ability of saccharin to make complex ions with the transition metal ions has been reported by some researchers [32–35]. If any of the water molecules in the hexaaquairon(II) complex can be replaced with a saccharin molecule, then any of the hypothetical octahedral complexes, illustrated in Fig. 13, might be formed [36].

To find out whether any of these hypothetical complexes or any other complex of Fe^{2+} ion with saccharin molecule (molecules) would be formed requires an

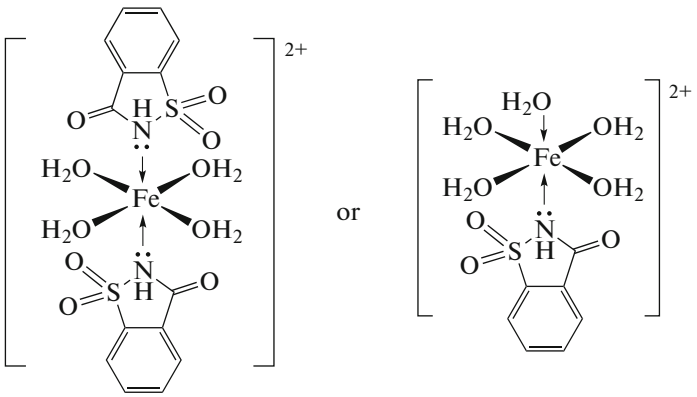

Fig. 13. Hypothetical aquairon(II) complexes with saccharin.

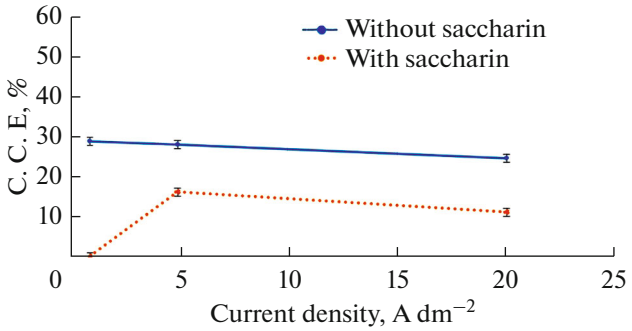

Fig. 14. Cathodic current efficiency of iron coatings obtained from baths with and without saccharin at 60°C and different current densities: 1, 5 and 20 A dm^{-2}.

extensive study which is outside the scope of the present investigation. Nevertheless, the results of this investigation showed that addition of saccharin to the bath for electrodeposition of iron is deleterious and leads to the instability of the bath. The UV-Vis spectrum (Fig. 6) of the bath with saccharin shifted to lower wavelengths, compared with the spectrum of the bath without saccharin. The maximum absorption wavelength (λ_{max}) was registered at 435 nm and the bath color changed, implying that some of the hexaaquairon(II) complex ions changed to a different type of a complex, perhaps, with saccharin molecules. A saccharin molecule has nitrogen and oxygen, hence, can act as strong filed ligand. Its imino group might be similar to ammonia with respect to its complex formation. Thus, it seems logical for it to have the maximum absorption wavelength lower than the maximum absorption wavelength of the hexaaquairon(II) complex [36].

Another deleterious effect of saccharin addition to the iron plating bath could be a possible reduction of saccharin on the cathode and its decomposition to benzamide and sulfur dioxide. If this reaction occurs, then the reduction of sulfur dioxide on the cathode surface in an acidic bath might produce hydrogen sulfide. The next reaction would be the reaction of hydrogen sulfide with the Fe^{2+} cation to produce iron sulfide if the solution contains iron(II) ions. These reactions and the formation of a metallic sulfide such as FeS in the electrodeposited CoFe coatings as well as the mechanism of the reaction have been extensively reported in [37]. Hence, the instability of the iron plating bath containing saccharin, under study in the present investigation, might be attributed to the decomposition reaction of saccharin.

The cathodic current efficiencies of the coatings are shown in Fig. 14. It is vivid that the maximum cathodic current efficiency was 28.4% at 1 A dm^{-2} for the bath without saccharin. However, the cathodic current efficiency for the bath with saccharin at the same current density was zero because deposits were not produced on the substrate. The maximum cathodic current efficiency for the bath with saccharin was 16% at 5 A dm^{-2}. According to the present results, for the samples without saccharin, the cathodic current efficiency of the deposits decreased when the current density increased. The cathodic current efficiency of the bath with saccharin also decreased when deposition took place at current densities higher than 5 A dm^{-2}.

Appearance

Figure 15 shows the appearance of iron coatings electrodeposited with different current densities. Appearance of the samples changed with increase of the current density from bright metallic, for the coatings obtained at low current densities (i.e. 1 and 5 A dm^{-2}), to mat, black, rough and non-metallic for the coatings produced at current densities higher than 10 A dm^{-2}. The formed iron oxide has low adhesion on the cathode surface (Fig. 15). Partially, oxide adheres to the cathode and a part of it spills into the solution so that it changes the color of the solution to black.

Appearances of the samples were studied at different current densities (i.e. 1, 5 and 20 A dm^{-2}) at 80°C and compared with those of the samples produced at 60°C. According to Fig. 16, at a low current density (1 A dm^{-2}), deposits with too many voids were produced formed via the reduction of hydrogen ions on the cathode. At 5 A dm^{-2}, the appearance was more metallic than deposits at 60°C. For the coatings obtained at a high current density (20 A dm^{-2}), the appearance changed from bright metallic to a dark and rough one.

Appearances of the samples deposited from a saccharin containing bath, were also studied at different current densities, i.e. 1, 5 and 20 A dm^{-2}. They changed with an increase of the current density. As seen in Fig. 17, deposits were not produced at a low current density (1 A dm^{-2}). At 5 A dm^{-2}, the appearance was dark metallic. For the coatings obtained at a high current density (20 A dm^{-2}), the appearance changed from dark metallic to dull, black, rough and non-metallic. As to the coatings produced at 5 and 20 A dm^{-2}, they were non-adherent to the substrate. This is contradictory to the results reported by others [24].

Surface Morphology

Figure 18 shows the surface morphology of iron coatings, with a uniform pyramidal structure for the samples electrodeposited up to 10 A dm^{-2}. From 15 to 25 A dm^{-2}, rough cauliflower morphologies were observed which were grown on the uniform pyramidal metallic structure. These different morphologies indicate that metallic iron coatings were electrodeposited at low current densities (i.e. 1, 5 and 10 A dm^{-2}). However, at high current densities (15, 20 and 25 A dm^{-2}) rough iron oxide coatings with cauliflower morphol-

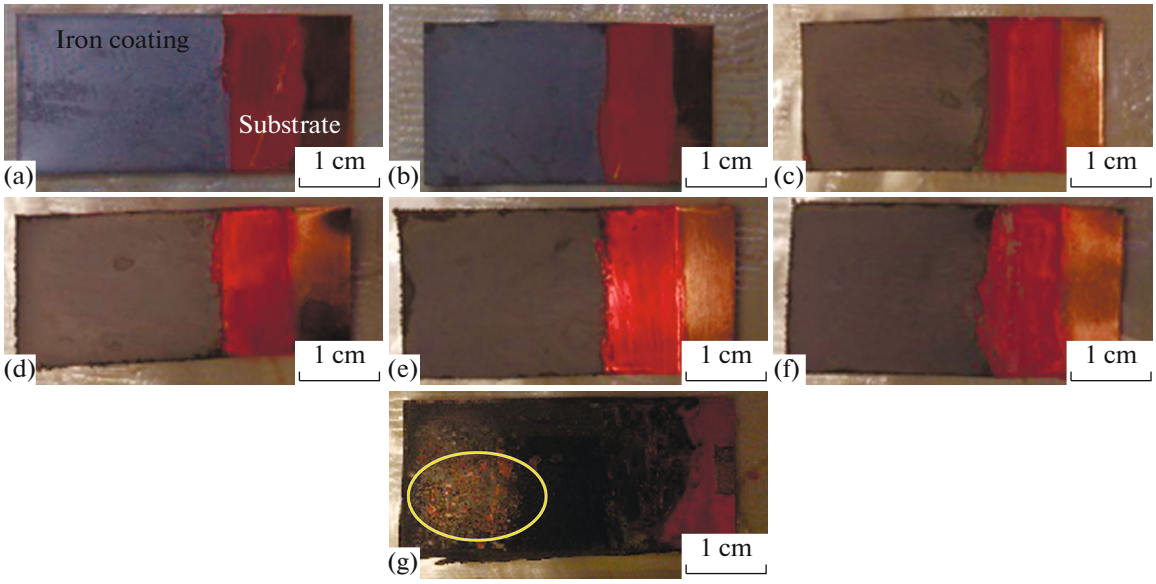

Fig. 15. Appearances of iron coatings obtained with different current densities at 60°C: (a) 1, (b) 5, (c) 10, (d) 15, (e) 20, (f) 25 A dm^{-2} and (g) low adhesion of iron oxide at high current (from 15 to 25 A dm^{-2}) densities on the cathode surface. The left sides of all the figures are the areas which were exposed to the electrolyte and the red color region was the lacquer to prevent exposure of the samples to the electrolyte.

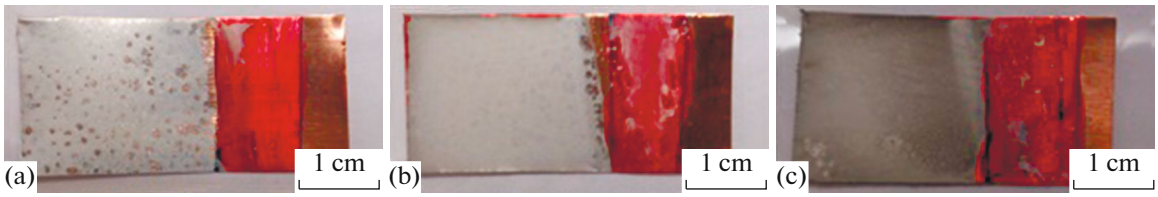

Fig. 16. Appearances of iron coatings obtained with different current densities at 80°C: (a) 1, (b) 5 and (c) 20 A dm^{-2}.

ogy were deposited. These morphologies are in good agreement with the Pourbaix diagram for iron. They are also in agreement with some recent reports [11, 23]. The results of the present research show that iron oxides are produced at high current densities.

Morphology of the samples was studied at three different current densities: 1, 5 and 20 A dm^{-2}, at 80°C and compared with that of the samples electrodeposited at 60°C. According to Figs. 18 and 19, at a low current density (1 A dm^{-2}) and 60°C, the morphology was uniform pyramidal but at 80°C, a platelet-like morphology was observed. The results at 5 and 20 A dm^{-2} showed that the structure was rough cauliflower for the samples electrodeposited at 60°C, but at 80°C, new larger platelets grew on the surface of the platelets previously formed at a low current density.

The surface morphology of the samples was studied at different current densities, i.e. 1, 5 and 20 A dm^{-2}, from a bath with saccharin at 60°C. At a low current density (1 A dm^{-2}), deposits were not produced on the substrate. This is in agreement with the XRD results obtained for the sample electrodeposited at the same

Fig. 17. Appearances of iron coatings deposited at different current densities and 60°C from bath with saccharin: (a) 1, (b) 5 and (c) 20 A dm^{-2}.

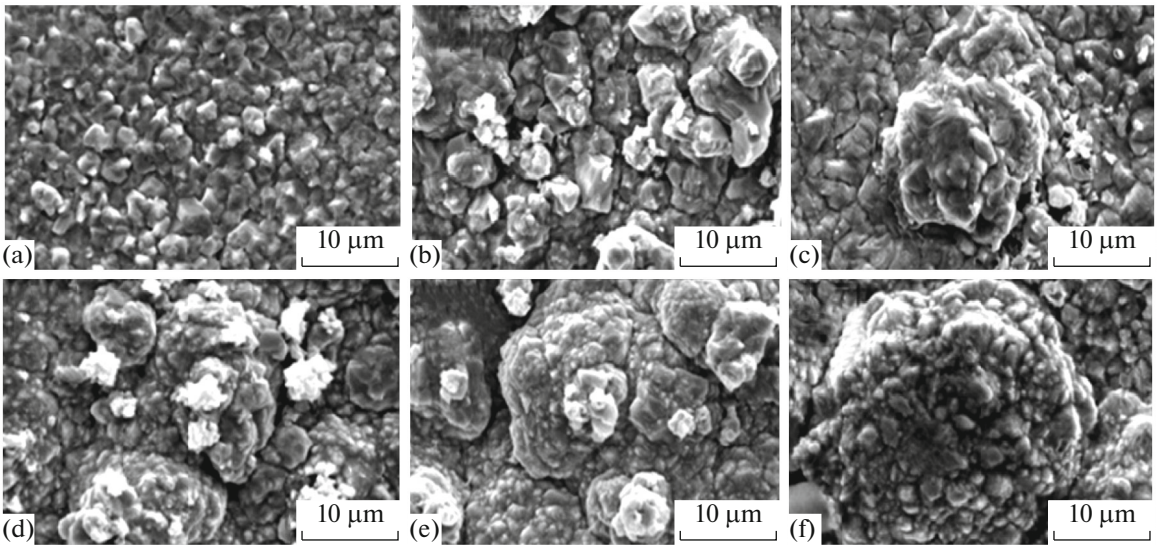

Fig. 18. SEM micrographs of iron coatings at 60°C: (a) 1, (b) 5, (c) 10, (d) 15, (e) 20 and (f) 25 A dm^{-2}.

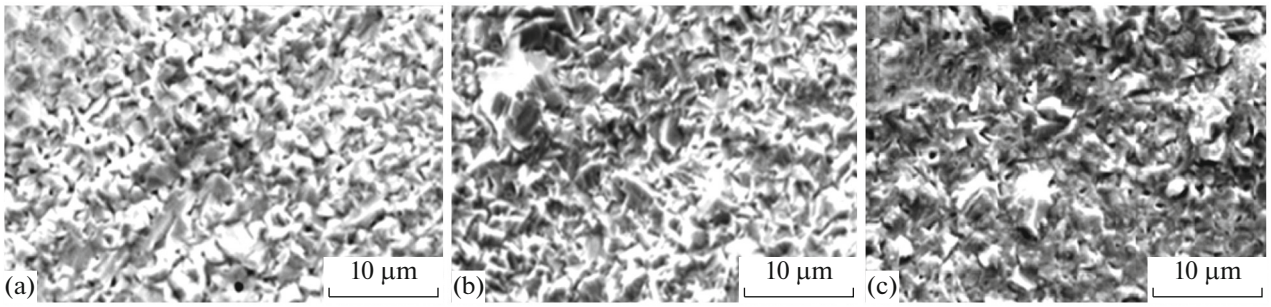

Fig. 19. SEM micrographs of iron coatings at 80°C: (a) 1, (b) 5 and (c) 20 A dm^{-2}.

current density. As seen in Figs. 18 and 20, the samples electrodeposited at 5 A dm^{-2} demonstrated the cauliflower morphology for the samples electrodeposited without saccharin. In contrast, the samples produced from the bath with saccharin had granular particulates. At 20 A dm^{-2}, the morphology of the samples electrodeposited from the bath without saccharin was rough cauliflower. The morphology of the sample prepared from a saccharin containing bath was also rough and dense cauliflower. It seems that small particles were attached on the surface of the deposit with the cauliflower morphology, as seen in Fig. 20b.

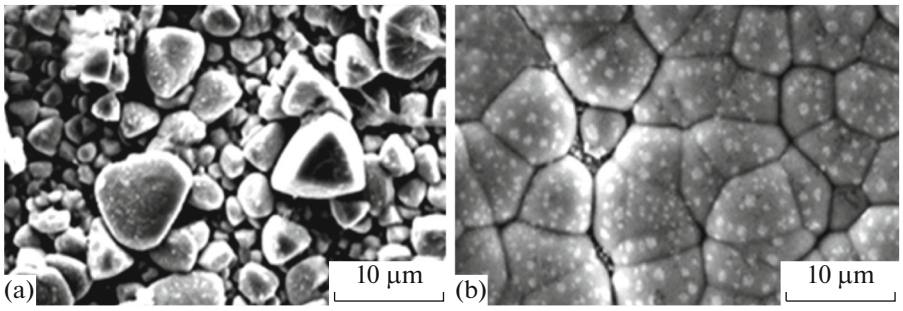

Fig. 20. SEM micrographs of iron coatings deposited from saccharin containing bath at 60°C: (a) 5 and (b) 20 A dm^{-2}.

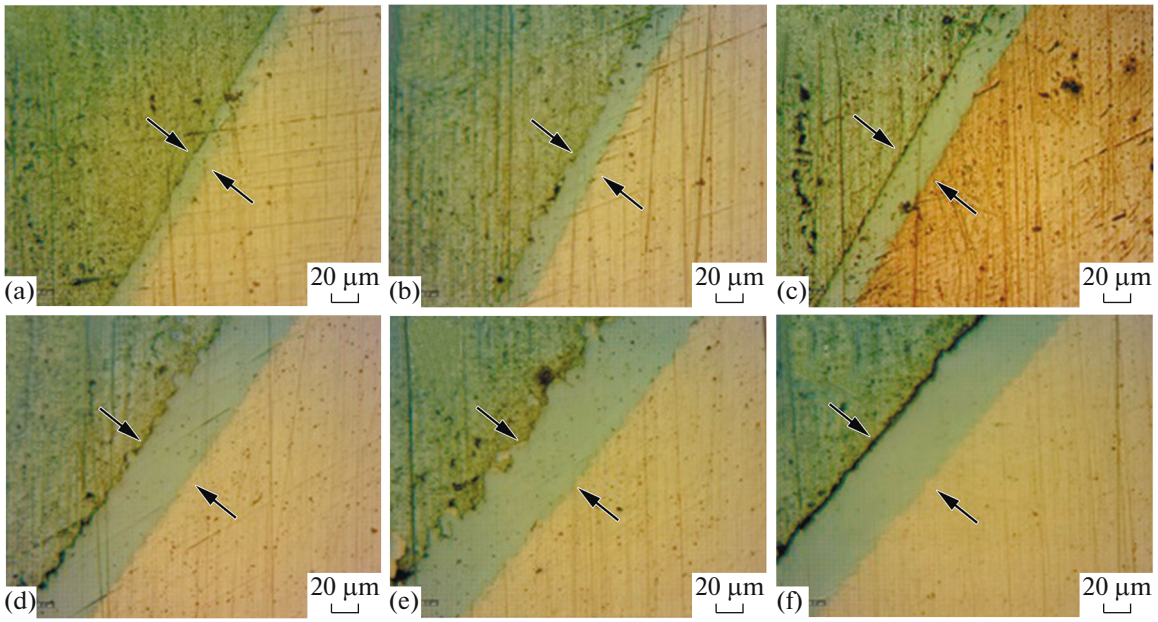

Fig. 21. Optical micrographs of cross sections of iron coatings obtained at 60°C and different current densities: (a) 1, (b) 5, (c) 10, (d) 15, (e) 20 and (f) 25 A dm^{-2}.

Thickness

The cross-sections of the coatings electrodeposited at different current densities illustrated an increase in the coating thickness with a higher current density (Fig. 21).

The growth rate increased for the samples electrodeposited at current densities up to 15 A dm^{-2}. A further increase in the current density retarded the growth rate (Fig. 22). The coatings obtained at 15 A dm^{-2} and higher current densities show the growth of a black oxide layer on the samples. This is seen profoundly for the sample deposited at 25 A dm^{-2}. The black oxide, grown on the sample surface, reduces electrical conductivity and prevents further growth of the metallic coating.

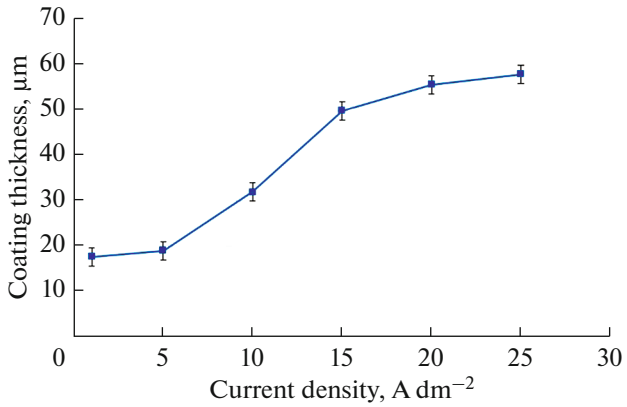

Fig. 22. Influence of different current densities on thickness of iron coatings at 60°C.

To investigate the effect of increasing tempe-rature on the coating thickness, optical microscopy images from the cross sections of the iron coatings obtained at 80°C, at different current densities (i.e. 1, 5 and 20 A dm^{-2}) were recorded and shown in Fig. 23. The cross sections of the electrodeposited coatings illustrated an increase in the coating thickness with current density.

On the other hand, when compared with the cross sections of the iron coatings deposited at 60°C, that are shown in Fig. 24, the results demonstrate that the growth rate of coatings at 60°C was higher than that at 80°C (Fig. 23).

The cross-sections of the coatings electrodeposited at different current densities, i.e. 1, 5 and 20 A dm^{-2} with saccharin could not be studied because the coatings were brittle and non-adherent to the substrate.

CONCLUSIONS

The conclusions are as follows: Nanocrystalline iron coatings with a variety of average grain sizes from different current densities (1 to 10 A dm^{-2}) at 60°C were successfully electrodeposited. UV-Vis spectroscopic analyses of the baths before and after electrodeposition showed that the iron(II) sulfate bath was unstable during electrolysis due to the formation of iron(III) complexes and iron(II) hydroxo complexes.

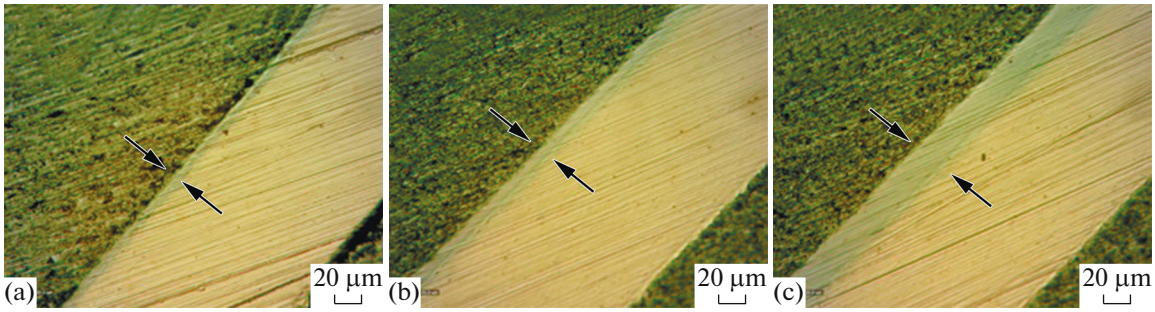

Fig. 23. Optical micrographs of cross sections of iron coatings obtained with different current densities at 80°C: (a) 1, (b) 5 and (c) 20 A dm^{-2}.

The bath color change during electrodeposition, especially at high current densities (10 to 25 A dm^{-2}), also indicated the instability of the iron(II) sulfate bath for electrodeposition of nanocrystalline iron coatings at 60°C. Increasing the bath temperature to 80°C during electrodeposition accelerated deterioration of the bath. Deterioration of appearances of the iron coatings, lowering cathodic current efficiency and also decrease of the coatings thickness at high current densities (10 to 25 A dm^{-2}) were the consequences of the bath instability, which had an impact on the coating morphology. Addition of saccharin to the bath was not beneficial for electrodeposition of nanocrystalline iron. The results showed that saccharin might act as ligand to form a complex ion with iron rather than as grain refiner. The results of the present investigation verified the fact that the iron(II) sulfate bath is unstable for electrodeposition of iron at high current densities, bearing in mind that employing high current densities is a requirement to produce nanocrystalline iron coatings. On the other hand, the bath may show a degree of stability if low current densities are used, albeit not for a long time.

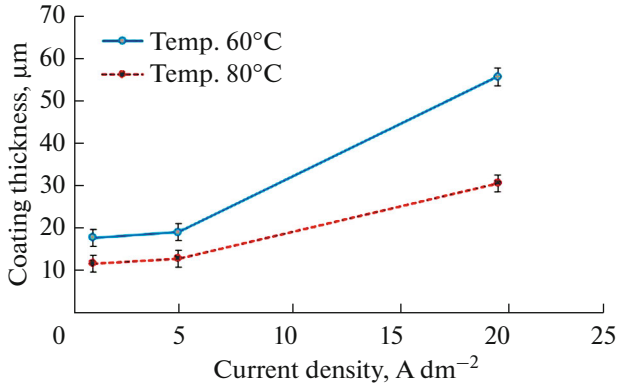

Fig. 24. Influence of different current densities (i.e. 1, 5 and 20 A dm^{-2}) on the thickness of iron coatings electrodeposited at two different temperatures.

ACKNOWLEDGMENTS

This research was supported by the research committee of Shiraz University. The authors acknowledge the financial support to Professor M.E. Bahrololoom. Special thanks to Dr. Zahra Ghaferi for her valuable discussion and help in the analysis of some results.

REFERENCES

1. Harty, S.F., McGeough, J.A., and Tulloch, R.M., *Surf. Technol.*, 1981, vol. 12, pp. 39–55.
2. Watanabe, T. *Nano Plating—Microstructure Formation Theory of Plated Films and a Database of Plated Films*, Amsterdam: Elsevier, 2004.
3. Kasper, C.H., *J. Res. Natl. Bur. Stand. (U.S.)*, 1937, vol. 18, pp. 535–541.
4. Zakirov, S.Z., *Met. Sci. Heat Treat.*, 1975, vol. 17, pp. 709–711.
5. Moravej, M., Prima, F., Fiset, M., and Mantovani, D., *Acta Biomater.*, 2010, vol. 6, pp. 1726–1735.
6. Moravej, M., Purnama, A., Fiset, M., Couet, J., and Mantovani, D., *Acta Biomater.*, 2010, vol. 6, pp. 1843–1851.
7. Gow, K.V., Iyer, S.P., Wu, H.H., Castelliz, K.M., et al., *Surf. Technol.*, 1979, vol. 8, pp. 333–346.
8. Jartych, E., Żurawicz, J.K., Maczka, E., and Borc, J., *Mater. Chem. Phys.*, 2001, vol. 72, pp. 356–359.
9. Koza, J., Uhlemann, M., Gebert, A., and Schultz, L., *J. Solid State Electrochem.*, 2008, vol. 12, pp. 181–192.
10. Schlesinger, M. and Paunovic, M., *Modern Electroplating*, New York: Wiley, 2011.
11. Inoue, K., Nakata, T., and Watanabe, T., *Mater. Trans.*, 2002, vol. 43, pp. 1318–1324.
12. Lai, S.H., McGeough, J.A., and Lau, P., *J. Mech. Work. Technol.*, 1978, vol. 1, pp. 231–243.
13. Diaz, S.L., Calderón, J.A., Barcia, O.E., and Mattos, O.R., *Electrochim. Acta*, 2008, vol. 53, pp. 7426–7435.
14. Afshari, V. and Dehghanian, C., *J. Appl. Electrochem.*, 2010, vol. 40, pp. 1949–1956.
15. Afshari, V. and Dehghanian, C., *Anti-Corros. Methods Mater.*, 2010, vol. 57, pp. 142–147. https://doi.org/10.1108/00035591011040100.

16. Afshari, V. and Dehghanian, C., *Int. J. Mater. Res.*, 2010, vol. 101, pp. 366–371.
17. Cotton, F.A., Wilkinson, G., Murillo, C.A., and Bochmann, M., *Advanced Inorganic Chemistry*, New York: Wiley, 1999.
18. Ballhausen, C.J. and Weiner, M.A., J. Electrochem. Soc., 1963, vol. 110, art. ID 97C.
19. Green, T.A., *Gold Bull.*, 2007, vol. 40, no. 2, pp. 105–114.
20. Green, T.A. and Roy, S., *J. Electrochem. Soc.*, 2006, vol. 153, pp. 157–163.
21. Lowinsohn, D., Alipázaga, M.V., Coichev, N., and Bertotti, M., *Electrochim. Acta*, 2004, vol. 49, pp. 1761–1766.
22. Tjandrawan, V. and Nicol, M.J., *Hydrometallurgy*, 2013, vol. 131, pp. 81–88.
23. Su, C.W., Yang, W., Guo, J.M., and Zhang, Y.J., *Vacuum*, 2012, vol. 86, pp. 2095–2101.
24. Zarpellon, J., Jurca, H.F., Klein, J.J., Schreiner, W.H., et al., *Electrochim. Acta*, 2007, vol. 53, pp. 2002–2008.
25. Evreinova, N.V., Shoshina, I.A., Naraev, V.N., and Tikhonov, K.I., *Russ. J. Appl. Chem.*, 2008, vol. 81, pp. 1180–1183.
26. Najafi Sayar, P. and Bahrololoom, M.E., *Trans. IMF*, 2009, vol. 87, pp. 246–253.
27. Najafi Sayar, P. and Bahrololoom, M.E., *J. Appl. Electrochem.*, 2009, vol. 39, pp. 2489–2496.
28. Rashidi, A.M. and Amadeh, A., *Surf. Coat. Technol.*, 2009, vol. 204, pp. 353–358.
29. Shirazi, S.H., Bahrololoom, M.E., and Shariat, M.H., *Surf. Eng. Appl. Electrochem.*, 2016, vol. 52, pp. 434–442.
30. Williamson, G.K. and Hall, W.H., *Acta Metall.*, 1953, vol. 1, pp. 22–31.
31. Delahay, P., Pourbaix, M., and van Rysselberghe, P., *J. Chem. Educ.*, 1950, vol. 27, p. 683.
32. Al Tanvir, T., Hossain, M.E., Al Mamun, M., and Ehsan, M.Q., *J. Bangladesh Acad. Sci.*, 2014, vol. 37, pp. 195–203.
33. Haider, S.Z., Malik, K.J., and Ahmed, K.J., *J. Bangladesh Acad. Sci.*, 1981, vol. 5, pp. 81–90.
34. Jovanovski, G., *Croat. Chem. Acta*, 2000, vol. 73, pp. 843–868.
35. Baran, E.J. and Yilmaz, V.T., *Coord. Chem. Rev.*, 2006, vol. 250, pp. 1980–1999.
36. Earnshaw, A. and Harrington, T.J., *Chemistry of the Transition Elements (Oxford Chemistry)*, Oxford: Oxford Univ. Press, 1973.
37. Tabakovic, I., Riemer, S., Tabakovic, K., Sun, M., et al., *J. Electrochem. Soc.*, 2006, vol. 153, pp. 586–593.